Materials Science in Semiconductor Processing 121 (2021) 105445

Contents lists available at ScienceDirect

Materials Science in Semiconductor Processing

journal homepage: http://www.elsevier.com/locate/mssp

Flexible, polymer-supported, ZnO nanorod array photoelectrodes for PEC water splitting applications

Tian-Feng Hou [a], Arunkumar Shanmugasundaram [a], Indrajit V. Bagal [b], Sang-Wan Ryu [b], Dong-Weon Lee [a,c,*]

[a] MEMS and Nanotechnology Laboratory, School of Mechanical Engineering, E Chonnam National University, Gwangju, 61186, Republic of Korea
[b] Department of Physics, Chonnam National University, Gwangju, 61186, Republic of Korea
[c] Center for Next-generation Sensor Research and Development, Chonnam National University, Gwangju, 61186, Republic of Korea

ARTICLE INFO

Keywords:
Flexible photoelectrode
Micropatterned substrate
PUA
ZnO NRs

ABSTRACT

An innovative ZnO based flexible photoelectrode was prepared on the micropatterned poly (urethane acrylate) (PUA) for efficient photoelectrochemical water splitting application. The micropatterned PUA was fabricated by the mold transfer process. A thin layer of Indium Tin Oxide was deposited on the PUA surface to give it surface conductivity and subsequently, one dimensional ZnO nanorods (NRs) arrays were prepared by a facile seed layer and hydrothermal method. The photocurrent density of the photoanode of ZnO NRs arrays deposited on the micropatterned PUA (ZP_M) was ~0.52 mA cm^{-2} at 1.23 V vs. RHE, which was ~3 times higher compared to that of ZnO NRs arrays deposited on the flat PUA (ZP_F). The improved performance of the ZP_M photoanode was attributed to the enhanced light capture capacity, excellent carrier collection ability, lower charge transfer resistance, and higher electrochemically active surface area.

1. Introduction

Recently, hydrogen generation from water has been considered the most appealing technology for sustainable energy [1]. Among several methods, the PEC water splitting is a promising technique due to its potential ability to convert solar energy into hydrogen [2]. Since Fujishima et al. [3] reported PEC driving water-splitting via a TiO_2 electrode in 1972, various functional electrodes have been explored for improving the PEC performance [4]. Over the years, several metal oxides, including TiO_2 [5], Cu_2O [6], Fe_2O_3 [7], $BiVO_4$ [8], and WO_3 [9], ZnO [10–13], have been obtained a wide range of investigation for PEC water splitting. Among them, ZnO has received significant attention owing to its non-toxicity, the strong oxidizing ability, excellent electrical transportability (carrier mobility (130–440 and 0.1–50 $cm^2\ V^{-1}\ s^{-1}$ for the electron (e^-) and hole (h^+), respectively [14]) and longer carrier diffusion length (130–440 nm [15]).

To date, various strategies were proposed to improve the PEC performance of the ZnO based photoelectrodes. For instance, loading ZnO with electrocatalyst, such as NiO, to promote oxygen evolution [16]; The incorporation of lower bandgap semiconductor material like Cu_2O [17], nitrogen doping [18], and quantum dot sensitizing [19] to improve overall absorbance and photo-response of the photoelectrode. Ding et al. prepared ZnO@CdS core-shell heterostructures and demonstrated in detail their enhanced photocatalytic and photoelectrochemical performance [20]. The morphology-controlling such as the fabrication of one-dimensional [21], textured porous plates [22] or three-dimensional (3D) branch structures [23] to enhance the utilization of minority carriers and light absorption. Finally, ZnO utilizes the piezoelectric effect to effectively separate and transfer the charge carriers, thus improving energy utilization efficiency [11,24,25].

The photoelectrodes have always been prepared on the conducting substrates such as silicon (Si), indium tin oxide (ITO), and fluorine-doped tin oxide coated glass plates [26,27]. Despite these substrates have superior transparency and conductivity, the glass substrate-based PEC devices' practical applicability met with limited success due to their expensive, fragile, and inflexible nature. Further, those substrates cannot be used to develop large scale roll-to-roll PEC devices [28]. To date, several research efforts have been devoted to developing intelligent, flexible water splitting photoelectrodes. For instance, Singh et al. fabricated a flexible PVDF/Cu/PVDF-$NaNbO_3$ photoanode, which

* Corresponding author. MEMS and Nanotechnology Laboratory, School of Mechanical Engineering, E Chonnam National University, Gwangju, 61186, Republic of Korea.
E-mail address: mems@jnu.ac.kr (D.-W. Lee).

https://doi.org/10.1016/j.mssp.2020.105445
Received 15 May 2020; Received in revised form 3 September 2020; Accepted 7 September 2020

showed a photocurrent density of ~1.37 mA/cm$_2$ [29]. Quynh et al. fabricated a flexible photoelectrode based on Fe_2O_3/ZnO/mica heteroepitaxy for PEC water splitting. The heteroepitaxial system's photocurrent density was ~5.5 and 3.0 times higher than those of pristine ZnO and Fe_2O_3, respectively [30]. Xiao et al. demonstrated in detail the boosted photoelectrocatalytic hydrogen evolution of a flexible CdS nanorods-carbon nanotubes/stainless steel mesh photoanode [31]. However, the complex processing technique required for those methods limits large scale fabrication of the PEC device. Further, the photoelectrodes' performance is also determined by other factors, such as structures in macro, micro or nanoscale, and interactions between complex components such as catalyst, semiconductor, and electrolyte. The most reported photoelectrodes were fabricated on a single-scale structure, which is not very effective in increasing the surface area compared to the micro- and nanoscale combined structure. Therefore, a suitable, cost-effective, and facile micro/nano-based fabrication strategies are highly desired to develop high-efficiency flexible photoelectrodes.

Herein, we demonstrate our successful attempt to fabricate ZnO-based photoelectrode on the ITO which was deposited poly (urethane acrylate) (PUA) flexible substrate. The surface area of the photoelectrode was improved by the formation of micropillars on the PUA surface. Then, 3D-branched ZnO nanostructures were prepared on the PUA micropillars. The photocurrent density generated by the ZnO grew on the ITO deposited micropatterned PUA (ZP_M) photoanode was ~0.52 mA cm^{-2} at 1.23 V vs. RHE. The ZP_M photoanode showed ~3 times higher photocurrent density than that of the ZnO grown on the ITO deposited flat PUA (ZP_F) photoanode. The proposed fabrication technique opens up a new way of designing flexible photoelectrodes on the patterned substrate for the PEC water splitting applications.

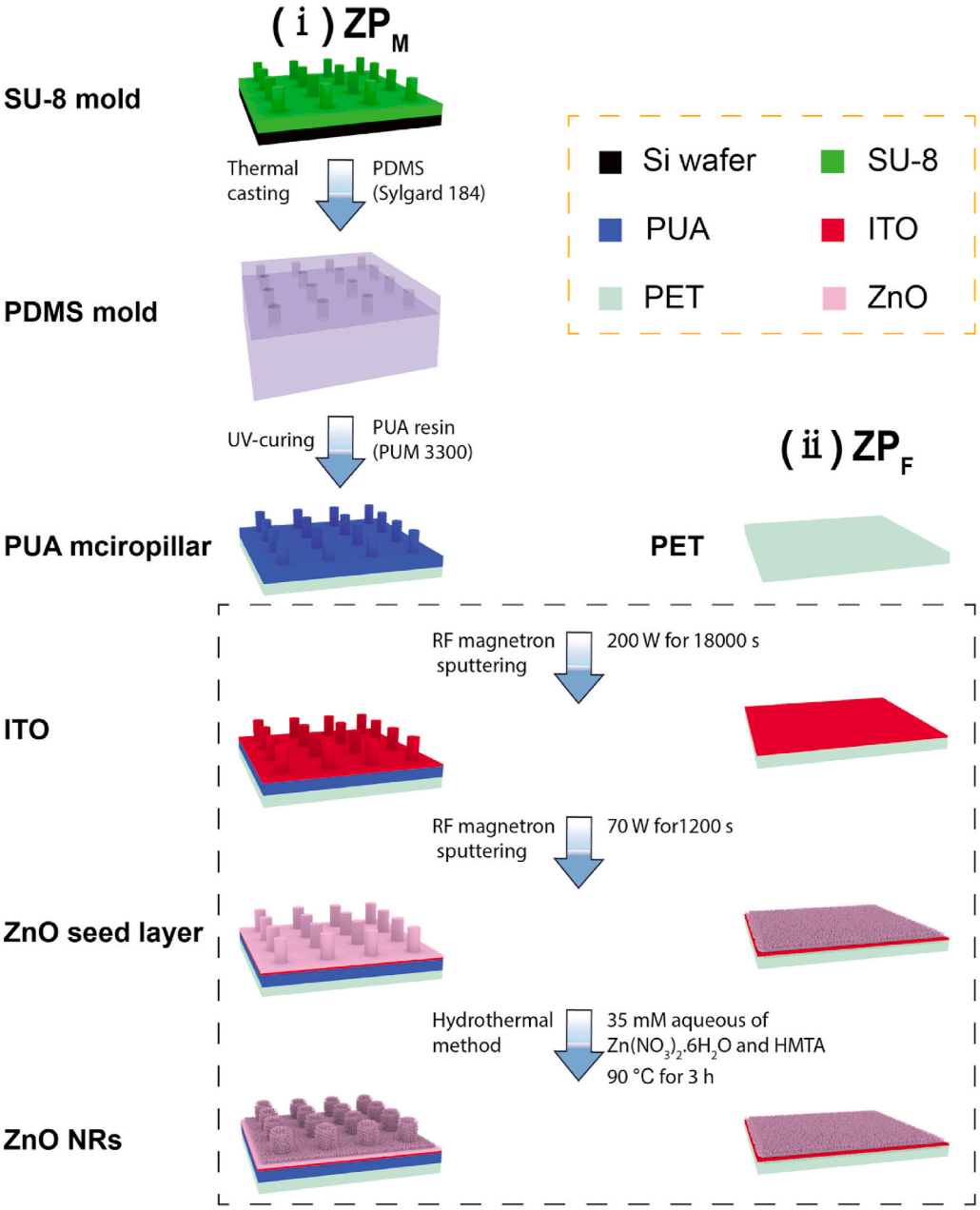

Scheme 1. The fabrication process flow of the flexible photoanodes based on ZnO decorated flat and micropatterned PUA and flat substrate.

2. Experimental section

2.1. Chemicals

Su-8 (3010, MicroChem), Polydimethylsiloxane (Sylgard 184, Dow Corning, Midland, MI, USA), PUA (PUM 3300, MC Net Co.). Targets of Indium Tin Oxide and ZnO in 4 inches were purchased from Kojundo Chemical Lab. Co., Ltd. Sodium sulfite (Na_2SO_4), Zinc nitrate ($Zn(NO_3)\cdot 6H_2O$), hexamethylenetetramine ($C_6H_{12}N_4$), sulfuric acid (H_2SO_4), hydrogen peroxide (H_2O_2), were purchased from Sigma-Aldrich Co. Ltd. All the chemicals are analytical reagent grade and used without any further purification.

2.2. Fabrication of the flexible micropatterned photoanode

Scheme 1 illustrates the fabrication process flow of the flexible micropatterned photoanode prepared on the micropatterned PUA and flat substrate.

2.2.1. Fabrication of SU-8 mold

Firstly, the SU-8 micropatterned mold was fabricated on the Si wafer through the modified photolithography process. In a typical fabrication process, the silicon wafer was cleaned by the piranha solution (H_2SO_4: H_2O_2 (2:1)) for 20 min and distilled water (DI), respectively. Then, the Si wafer was dried using the nitrogen flow. Subsequently, the Si wafer was dehydrated on the hotplate at 150 °C for 30 min. The 20 μm thick SU-8 was spin-coated on the silicon wafer and then soft baked on a hot plate at 95 °C for 10 min. After the baking process, the substrate was naturally cooled down to room temperature. Next, the micropillar was formed on the SU-8 surface through a patterned Chromium mask using a mask aligner (MDA-400-IR) under the UV illumination (150 mL/cm^2) followed by baking on a hot plate at 95 °C for 3 min. Finally, the micropatterned SU-8 was realized by immersing the sample in a developer solution (MicroChem's SU-8 Developer).

2.2.2. Fabrication of PDMS mold

The PDMS mixture was prepared by mixing it's base and curing agent in a ratio of 10:1. Then, the mixture was kept in a vacuum desiccator (F42025) for 30 min for degassing. Subsequently, the PDMS was poured on the μ-patterned SU-8 positive mold and degassed for 30 min. Next, the PDMS with SU-8 mold was cured at 80 °C for 4 h on a hotplate in an atmospheric condition. Finally, the PDMS negative mold was peeled off from the SU-8 mold.

2.2.3. Preparation of a PUA micropillar

In a typical fabrication process, 1 mL of UV-curable PUA resin was dispensed onto the PDMS mold. Then, a ~100 μm thick PET supporting film was brought in contact with the PUA resign by gentle pressing. The micropatterned PUA film formed on the PDMS mold by gently rolling a roller over the PET film's top surface. The bubbles in the PUA mixture were expelled out during the rolling process. Then, the PUA with PDMS mold was exposed to UV light (180 mJ cm^{-2}). After curing, the micropatterned PUA film was released from the PDMS mold.

2.2.4. ITO deposition on the PUA surface

The conductive ITO was deposited on the μ-pillar patterned PUA surface by an RF magnetron sputtering at room temperature. In a conventional sputtering process, a 99.9% pure ITO was used as source material. The base pressure was fixed $<5 \times 10^{-6}$ Torr. The pressure and flux of Ar were ~5 mTorr and 20 sccm, respectively. The ITO was deposited on the micropatterned PUA surface for 5 h at a deposition power of 70 W. The ITO layer was also deposited on the PET to make a flat substrate for ZnO NRs growth.

2.2.5. Preparation of the ZnO NRs on the ITO coated PUA surface

The one-dimensional ZnO NRs were grown on the ITO deposited flat substrate, and micropatterned PUAs surface by a simple two-step fabrication technique. In a typical fabrication process, firstly ZnO seed layer was formed on the ITO deposited surface by an RF magnetron sputtering at room temperature. A 99.9% pure ZnO target was used as source material for the ZnO seed layer deposition. The Ar gas was used as the working gas with a 5 mTorr pressure and 20 sccm flux. The ZnO seed layer was deposited for 20 min at a power of 70 W. Then, ZnO NRs arrays were grown by a facile hydrothermal method [32]. In a typical hydrothermal method, 35 mM of $Zn(NO_3.\ 6H_2O)$ was dispersed in a 50 mL of distilled water under constant magnetic stirring. Then, 35 mM of HMTA was added to the above solution to get the desired reaction mixture. After forming a clear solution, the mixture was transferred to the stainless steel autoclave. The ZnO seed layer deposited substrate was placed at 45° against the wall of the autoclave. The autoclave was then placed in a programmable oven and heated to 90 °C at the heating rate of 5 °C/min and maintained at that temperature for 3 h. After the hydrothermal reaction, the ZnO NRs arrays coated film was taken out from the reaction medium and washed by deionized water. Finally, the sample was dried in an oven at 60 °C for 2 h.

2.3. Characterization of the photoanodes

The properties, such as morphology, element distribution, structural characteristic, crystalline structure, and surface composition of as-prepared photoanodes were analyzed with field-emission scanning electron microscopy (FE-SEM, Phillips XL30S), energy-dispersive X-ray spectroscopy (EDX, Oxford Instruments), transmission electron microscope (TEM, JEM-2100F), X-ray powder diffraction (XRD, Rigaku), X-ray photoelectron spectroscopy (XPS; Multilab 200), and attenuated total reflection Fourier-transform infrared (ATR-FTIR) analysis. The specific surface area of the fabricated electrodes was investigated by the Brunauer–Emmett–Teller (BET) surface area. The Raman spectra were measured and collected using a 515 nm Diode laser with a LabRam HR800 UV Raman microscope (Horiba Jobin-Yvon, France). The range of Raman shift was 50–1000 cm^{-1}. Room-temperature

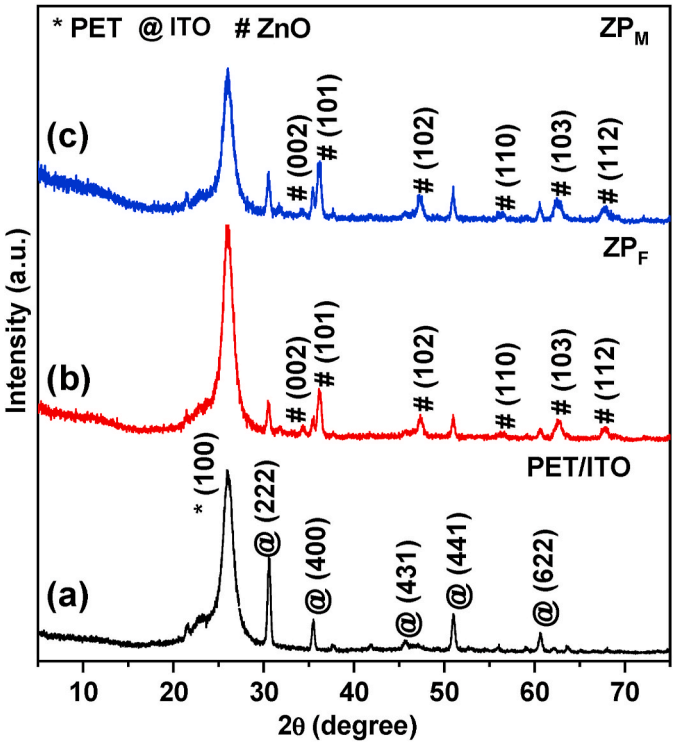

Fig. 1. (a–c) The powder XRD patterns of the fabricated ZP_F and ZP_M along with the bare ITO coated PET substrate.

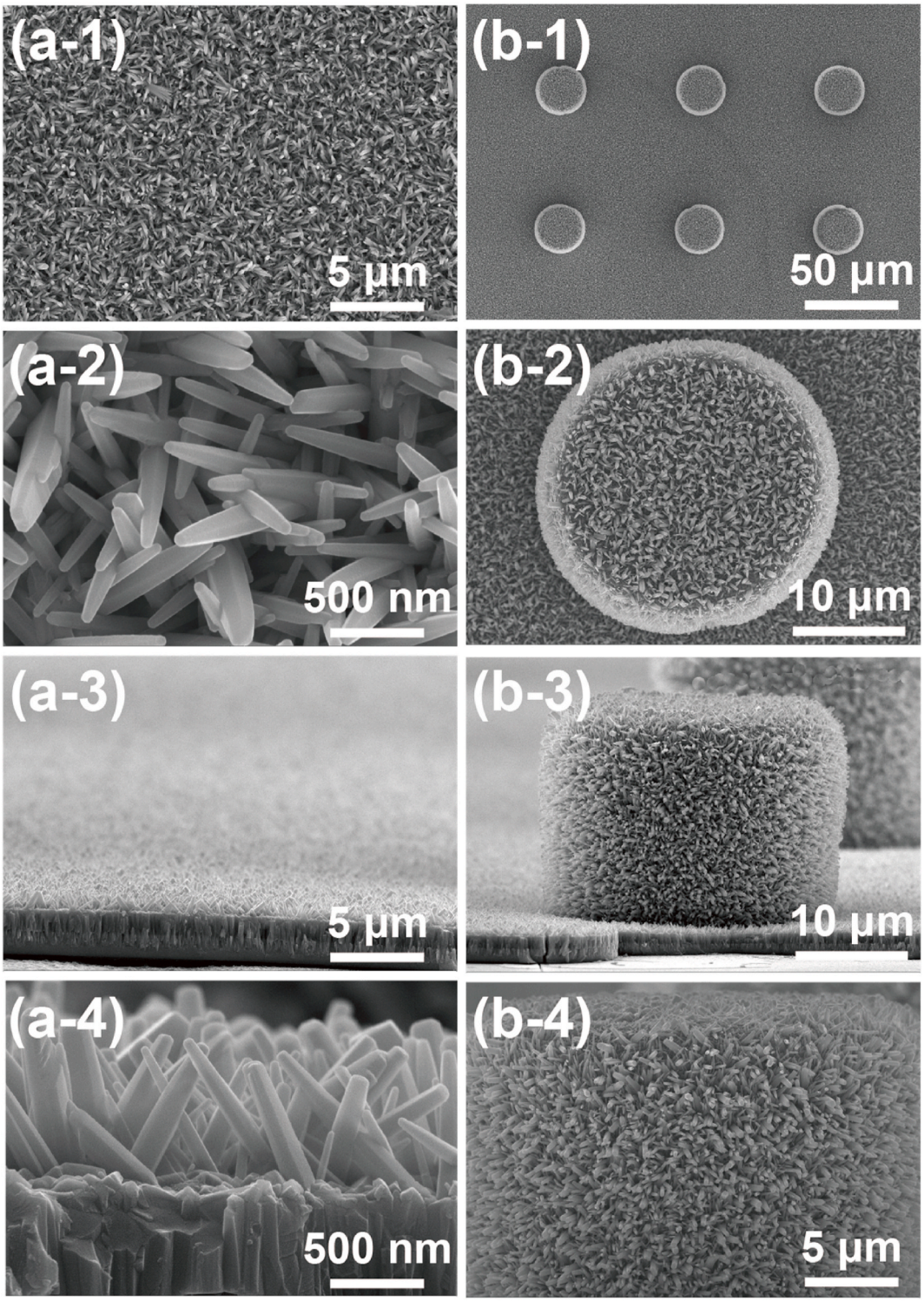

Fig. 2. The morphology of the fabricated ZP_F and ZP_M films at different magnifications. (a-1, a-2) top and (a-3, a-4) cross-section view of the prepared ZP_F, (b-1, b-2) top and (b-3, b-4) cross-section view of the prepared ZP_M.

photoluminescence (PL) spectroscopy was carried out with a spectrometer (f = 0.5 m, Acton Research Co., Spectrograph 500i, USA) and an intensified CCD(PI-MAX3) (Princeton Instrument Co., IRY1024, USA) equipped with a He–Cd laser which excitation wavelength is 325 nm. The ultraviolet diffused reflectance spectra (UVDRS) analysis was conducted on a Cary 300 UV–Vis. The UV–vis absorption function (F(R)) of the materials was estimated from the corresponding diffuse reflectance spectra (DRS) using the Kubelka–Munk equation (Eq. (S1)) as shown in the Supplementary Material.

2.4. Photoelectrochemical and electrochemical measurements

The PEC water splitting performance of the as-prepared photoanodes was analyzed with a three-electrode quartz electrochemical cell equipped with an electrochemical workstation. A Pt wire and Ag/AgCl were used as the counter electrode and the PEC cell's reference electrode,

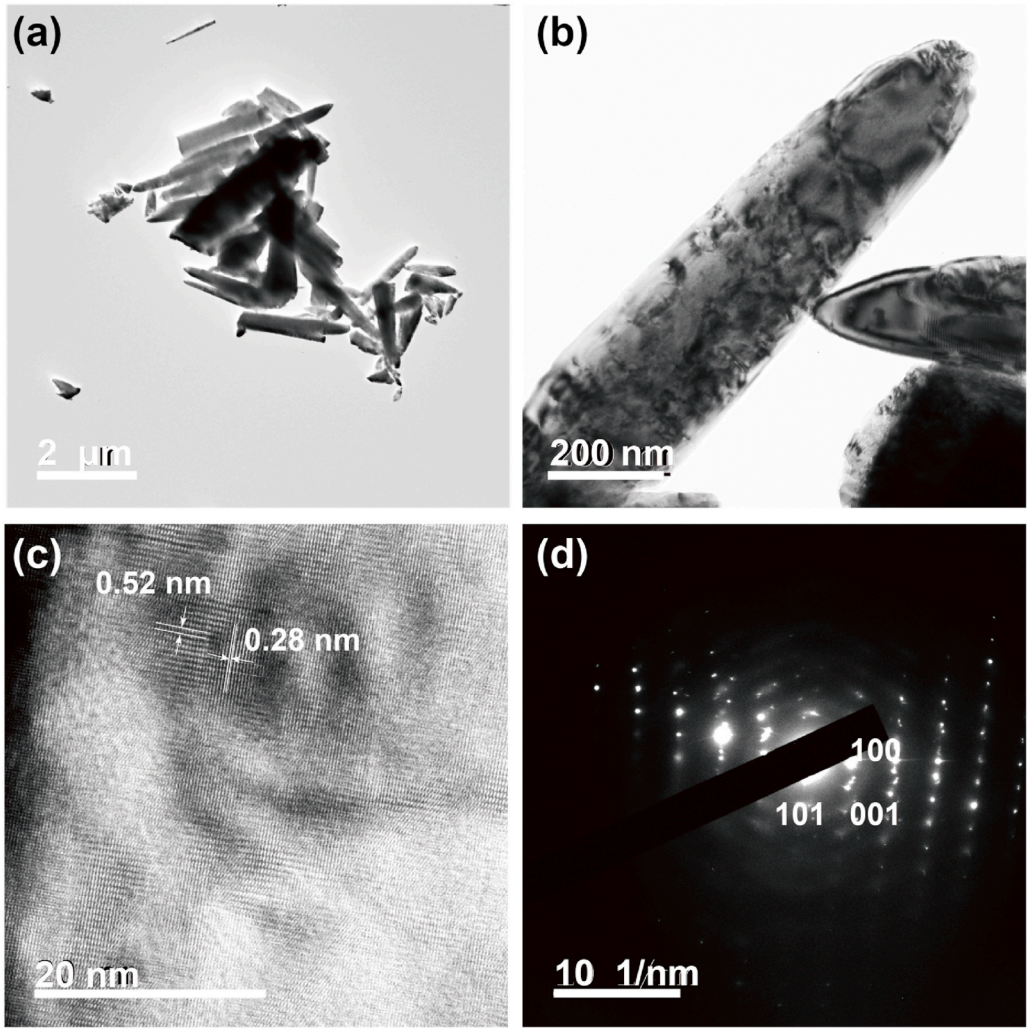

Fig. 3. (a, b) TEM images of the as-prepared ZP_M at two different magnifications, (c, d) high-resolution transmission electron micrograph and the corresponding SAED pattern of the as-prepared ZP_M.

respectively. The conversion of the potential in the Ag/AgCl and RHE was shown in Eq. (S3) and Eq. (S4). The exposed area of the as-fabricated photoanodes is 0.5 cm^2. The water splitting process was performed in the electrolyte of 0.5 M Na_2SO_4 (pH ~7.0) and irradiated with visible light provided by 300 W Xenon Arc lamp (Newport, model 69,911 Xenon Supply) coupled with an AM 1.5G filter. The calibrated power density of the illuminated light is 100 mW/cm^2. The incident photon-to-current conversion efficiency (IPCE) was measured with a three-electrode configuration at 0.6 V vs. RHE using Xenon Arc lamp equipped with a monochromator (Newport). A chopper was placed in front of the monochromator. The valued was calculated by IPCE (%) = 100 × (1240 i_{ph})/(λI_{light}), where 1240 represents the product of the speed of light and Planck's constant, i_{ph} is the photocurrent density (mA cm^{-2}), λ is the wavelength (nm) of the incident light, and I_{light} (mW cm^{-2}) is the intensity of light source at each wavelength. The electrochemical impedance spectroscopy (EIS) was conducted in the same electrolyte with the frequency from 10^5 to 10^{-1} Hz using an amplitude of 10 mV at the open circuit potential in the dark condition.

3. Results and discussion

The crystal structure and phase purity of the fabricated ZP_F and ZP_M photoelectrodes were analyzed by the powder X-ray diffraction (XRD) analysis. Fig. 1 shows the powder XRD pattern of the as-prepared ZP_F and ZP_M along with the bare PET/ITO substrate. The diffraction pattern at 2θ of ~25.9° attributed to the (100) crystal plane of PET (Fig. 1(a)) [33]. The diffraction pattern observed at 2θ of ~30.6°, 35.4°, 50.9°, and 60.6° could be indexed to the (222), (400), (441), and (622) crystal planes of ITO (Fig. 1(a)) [34]. The diffraction pattern observed at 2θ of ~34.2°, 36.1°, 47.2°, 56.2°, 62.6°, and 67.8° could be indexed to the (002), (101), (102), (110), (103) and (112) crystal planes of wurtzite ZnO crystal structure (JCPDS Card no.36–1451) (Fig. 1(b and c)) [32, 35]. The strong diffraction pattern at 36.1° corresponding to the (101) plane indicating the c-axis growth of the ZnO nanorods. The calculated lattice parameters a = b and c of the fabricated ZP_F and ZP_M photoelectrodes were ~0.331 nm and 0.528 nm and ~0.328 and 0.529 nm, respectively. The calculated lattice parameters are exactly matched with the reported value of the wurtzite ZnO crystal structure [35]. The crystallite size of the ZP_F and ZP_M photoelectrodes was estimated full width at half maximum of the X-ray diffraction pattern using the Scherrer's formula [36]. The ZP_F and ZP_M photoelectrodes' average crystallite size was found to be ~16 and 19 nm, respectively.

The morphologies of the fabricated ZP_F and ZP_M films were analyzed by the electron microscope through scanning and transmission mode. Fig. 2 shows the FE-SEM images of the fabricated flexible ZP_F and ZP_M photoelectrodes at different magnifications. Fig. 2a(1–4) show the top view and cross-sectional view of the ZP_F. Fig. 2b(1–4) show the FE-SEM images of the top view and cross-sectional view of the ZP_M. As observed, the 1D ZnO NRs arrays were uniformly grown on the entire surface of ITO deposited on the flat substrate and micropatterned PUA surfaces.

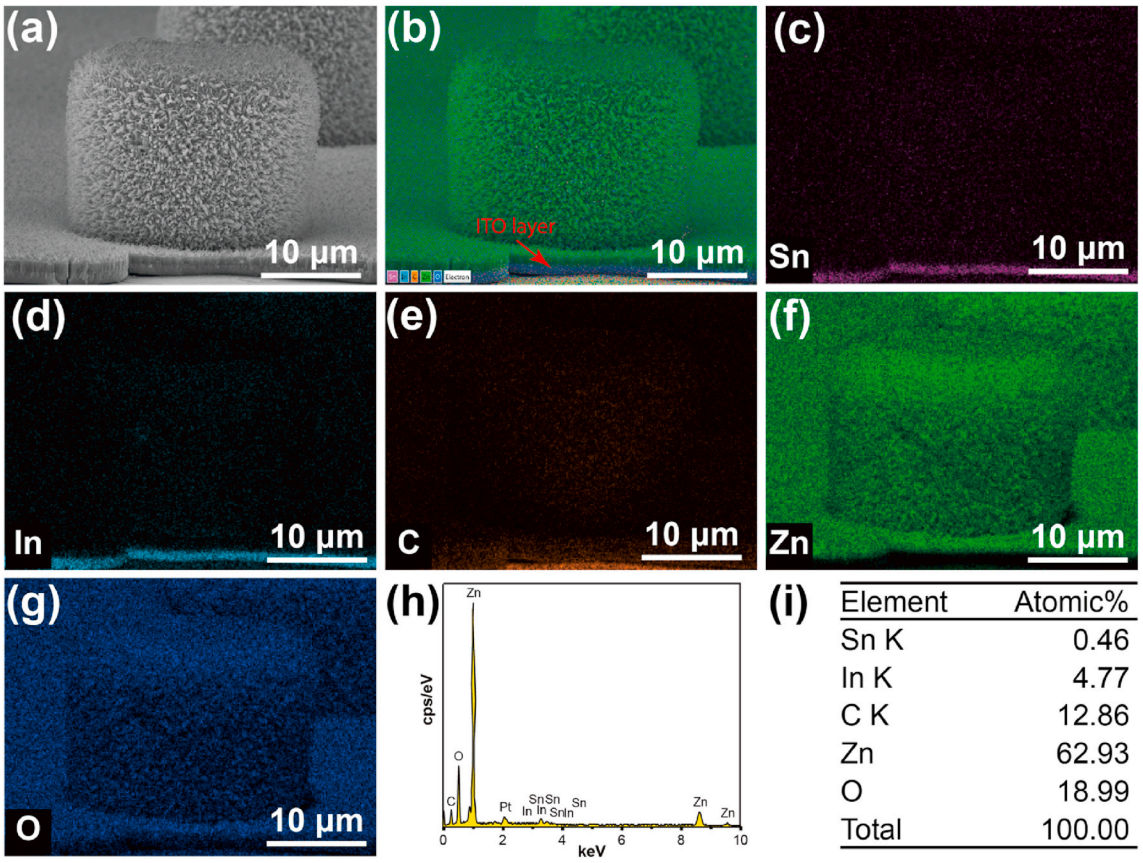

Fig. 4. Elemental mapping of the fabricated ZP_M film. (a) The FE-SEM image is showing the ZnO NRs on the micropatterned PUA, (b) merged image combing all element mapping, (d–i) the corresponding EDS mapping of Sn, In, C, Zn, and O, respectively, (h and i) the energy dispersive spectrum of the fabricated ZP_M and the quantitative elemental percentages.

The dimensions of the ZnO NRs were found to be ~100 nm in diameter and ~1 μm in length. Further, Fig. 2(b-1, and b-2) show the PUA micropillars with a diameter of ~20 μm and a height of ~20 μm. The distance between the micropillars is ~70 μm. Each micropillar was completely and uniformly covered by the ZnO NRs to form 3D branched morphology, which was clearly confirmed by the cross-section view (Fig. 2b(1–4)).

The as-prepared ZP_M was further characterized by the TEM analysis. The as-prepared ZnO NRs were scratched from the PUA surface and dispersed in ethanol solution using ultrasonication. Fig. 3(a) shows the low magnified TEM image of the as-prepared ZnO, demonstrating the obtained material's 1D nature. The high magnified image in Fig. 3(b) shows the as-prepared a whole ZnO NRs. The high-resolution TEM (HR-TEM) shows the lattice fringes with the spacing of 0.52 nm and 0.28 nm which were attributed to the (001) and (100) planes of the hexagonal wurtzite ZnO crystal structure, respectively (Fig. 3(c)) [37,38]. The selected area electron diffraction (SAED) pattern shows the Lawe spots indicating the high crystalline quality of the as-prepared ZnO NRs. The SAED patterns could be indexed to the (100), (001) and (101) plane of the wurtzite ZnO crystal structure (Fig. 3(d)) [36].

The fabricated ZP_M film's elemental composition was investigated by the energy dispersive spectrum (EDS) and elemental mapping analysis. Fig. 4(a) shows the FE-SEM images of the ZnO NRs arrays coated PUA micropillar. The merged elemental mapping image shows that the ZP_M film consists of elements of Sn, In, C, Zn, and O, and a distinct thin layer of ITO on the PUA surface (Fig. 4(b)). Fig. 4(c–g) show the individual elemental mapping of the ZP_M film. The homogenous distribution of Sn, In, C, Zn, and O indicated the hybrid PUA/ZnO composite's uniform formation. The EDS spectrum of the ZP_M (Fig. 4(h)) shows the electron peaks from Sn, In, C, Zn, and O, combined with Pt, which came from the conductive layer coating deposited in the sample preparation. The atomic percentages of the Sn, In, C, Zn, and O, in the ZP_M, were found to be ~0.46, 4.77, 12.86, 62.93, and 18.99, respectively.

The as-prepared ZP_M film was further characterized by the XPS analysis (Fig. 5). The survey spectra show the photoelectron peaks from Zn, O, and C. No other photoelectron peaks were observed, indicating the phase pure formation of the as-prepared sample (Fig. 5(a)). Fig. 5(b) shows the high-resolution core-level spectrum of the ZnO in the Zn 2p region. The spin-orbit split observed at ~1022 and 1045 eV corresponds to the Zn $2p_{1/2}$ and Zn $2p_{3/2}$, respectively. The binding energy difference between the Zn $2p_{1/2}$ and $2p_{3/2}$ was ~23.14 eV [39]. This evidently illustrates that the chemical valence of Zn is in the +2 oxidation state in ZnO. Fig. 5(c) shows the core-level spectrum of the carbon in the C1s region. The carbon peak was deconvoluted into four peaks depending on its chemical state. The peak at 283.32 eV was attributed to the formation of C–Zn. The photoelectron peak at 284.6 eV was due to the C–C bond. The other two peaks located at 285.75 and 288.59 eV were indexed to the presence of C–O–C and O–C═O bond [40]. Fig. 5(d) shows the photoelectron peaks of oxygen in the O1s region. The O1s peak was deconvoluted into three peaks depending on its oxidation states. The photoelectron peak at 529.63 eV was ascribed to the O^{2-} ion in the wurtzite structure, which were encompassed by the Zn atoms with their full complement of nearest-neighbor O^{2-} ions. Further, the photoelectron peak is much stronger than the other two binding energy peaks, indicating that most of the oxygen exists in the ZnO was lattice oxygen O^{2-}, thus the obtained ZnO shows high crystalline as confirmed by the XRD shown in Fig. 1. The peak at 530.68 eV was due to the surface oxygen species (O^{2-} ions) in the anoxic region of the ZnO matrix, indicating that there were oxygen vacancies in the ZnO [41]. Another binding energy at 531.72 eV can be indexed to the surface adsorbed

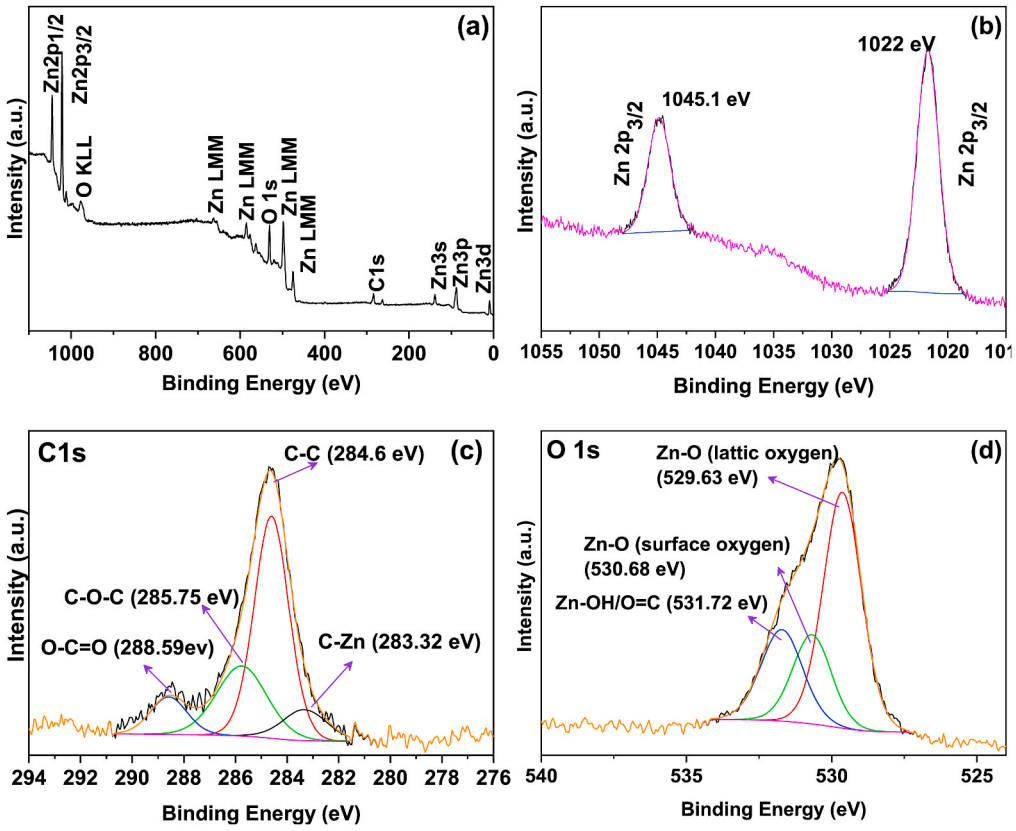

Fig. 5. XPS analysis of the as-prepared ZP_M film. (a) Survey spectrum, and high-resolution core-level spectra of the as-prepared (b) Zn2p, (c) C1s, and (d) O1s region of the as-prepared ZP_M.

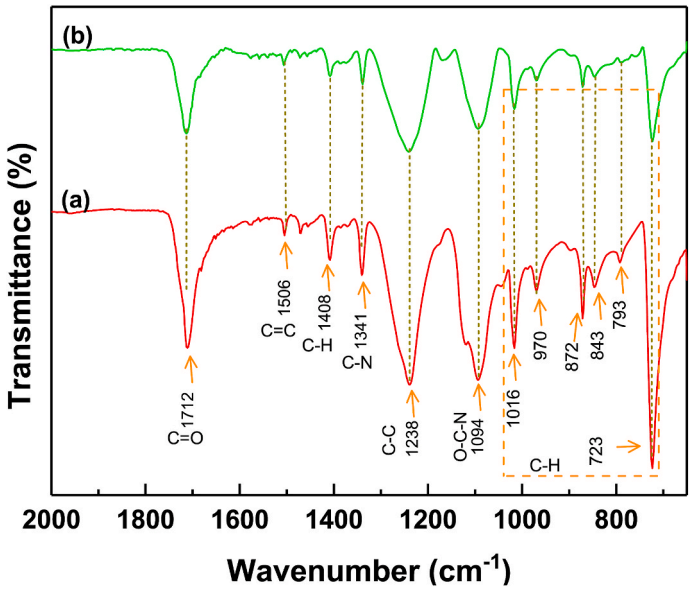

Fig. 6. The ATR-FTIR spectra of the fabricated flexible (a) ZP_F and (b) ZP_M films.

oxygen species and OH on the surface of ZnO [42].

The as-prepared ZP_F and ZP_M films were further investigated by the ATR-FTIR analysis (Fig. 6). Both the flexible films were showed similar fundamental vibrational modes. The absorption band at 592 and 433 cm^{-1} was attributed to the In–O bond [34] and Zn–O stretching vibrations [43], which were not observed in our materials experimental limitation of the instrument used for the analysis. The fundamental vibrational modes seen at 723, 793, 843, and 872 cm^{-1} were associated with the aromatic C–H out-of-plane bending. The adsorption band at 970 and 1016 cm^{-1} were assigned to the C–H in-plane bending. The band at 1094 cm^{-1} could be indexed to the stretching vibrations of the OCN functional group. The peak at 1238 cm^{-1} was attributed to the skeletal C–C vibrations. The vibrations observed at 1341 and 1408 cm^{-1} were due to C–N and C–H's stretching and bending vibrations, respectively. The vibrational bands at 1506 and 1712 cm^{-1} were assigned to the aromatic ring stretching (C═C–C) and the C═O stretching in a

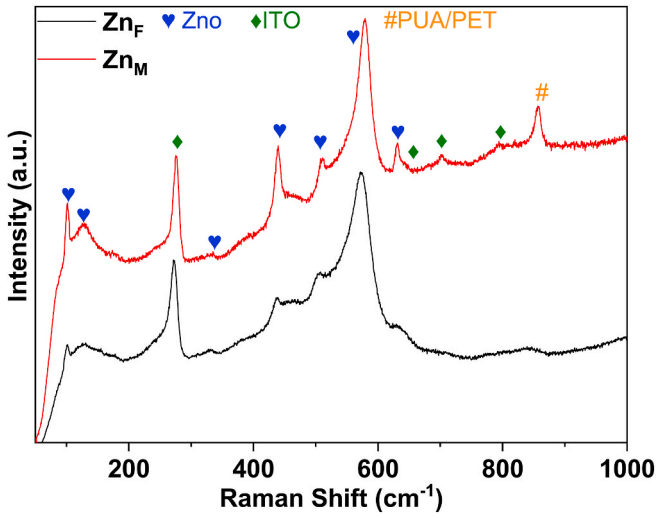

Fig. 7. The Raman spectra of the fabricated flexible ZP_F and ZP_M photoelectrodes.

carboxylic acid (-COOH), respectively [44].

The crystal structure and phase purity of the fabricated photoelectrodes based on the ZP_F and ZP_M photoelectrodes were investigated using the Raman spectra analysis (Fig. 7). The as-prepared samples showed several Raman active phonon and phonon combinations modes which can be assigned to the wurtzite ZnO crystal structure. The Raman band observed at 99.8 and 437.7 cm^{-1} can be indexed to the $E_2^{(low)}$ (E_{2l}), and $E_2^{(high)}$ (E_{2h}) modes, respectively, which were associated with the Zn sublattice [45]. The $E_2^{(high)}$ is associated with the motion of oxygen atoms, $E_2^{(low)}$ is associated with a zinc sublattice. The Raman band observed at 573 cm^{-1} can be indexed to the first-order Raman scattering corresponding to the longitudinal optical phonon mode A_l(LO). The peak at 329.5 cm^{-1} is due to the second-order structure arising from the fundamental overtones or the combination of $E_2^{(high)}$ - $E_2^{(low)}$. The Raman band at 507.1 cm^{-1} attributed to the multiphoton process of E_1(TO)+E_{2l} (transverse optical (TO)) [46]. The Raman band observed at 190 cm^{-1} is due to the interstitial zinc (Zn_i) while the peak at 620 cm^{-1} attributed to the defects related to the presence of oxygen vacancy (V_o) in the samples. The strong vibration absorption peak at 576 cm^{-1} can be indexed to the combination of A_1(LO) and V_o [47]. The other bands observed at 276, 631, 702.6, 793.5, 839.1, and 857.2 cm^{-1} can be indexed to the optical phonon modes arising from the ITO and PUA/PET substrate.

The optical properties of the fabricated ZP_F and ZP_M films were investigated by the UVDRS analysis at absorbance mode at wavelength in the range of 300–800 nm (Fig. 8(a)). The ZP_F showed an absorption edge at ~380 nm whereas, the ZP_M showed the band edge at ~390 nm. The ZP_M exhibited a higher absorption intensity at the UV region comparing to that of ZP_F. The optical bandgap of the ZP_F and ZP_M were estimated from Tauc plots (Fig. 8(b)) with Eq. (S2). The calculated bandgap of the ZP_F and ZP_M was ~3.27 and 3.15 eV, respectively.

The surface area and pore size distribution of the fabricated

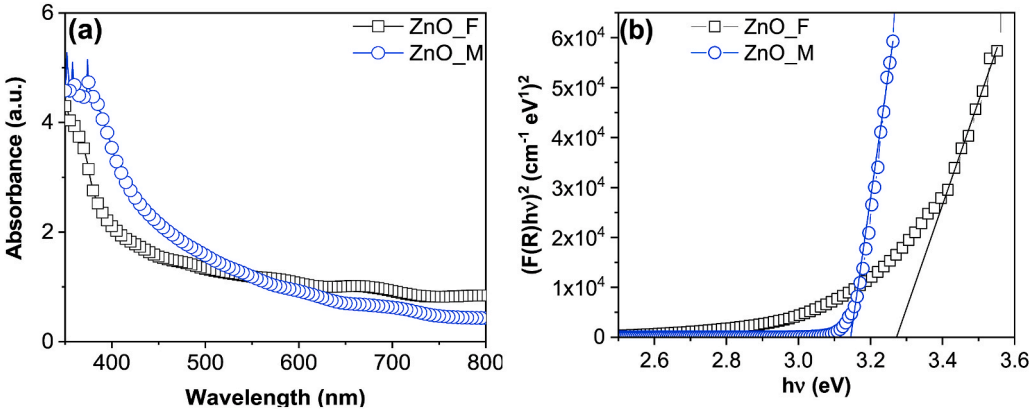

Fig. 8. The UV–Vis absorption spectra of the as-prepared flat and micropillar photoanodes, and (b) corresponding Tauc plots of $(F(R)h\nu)^2$ versus photon energy.

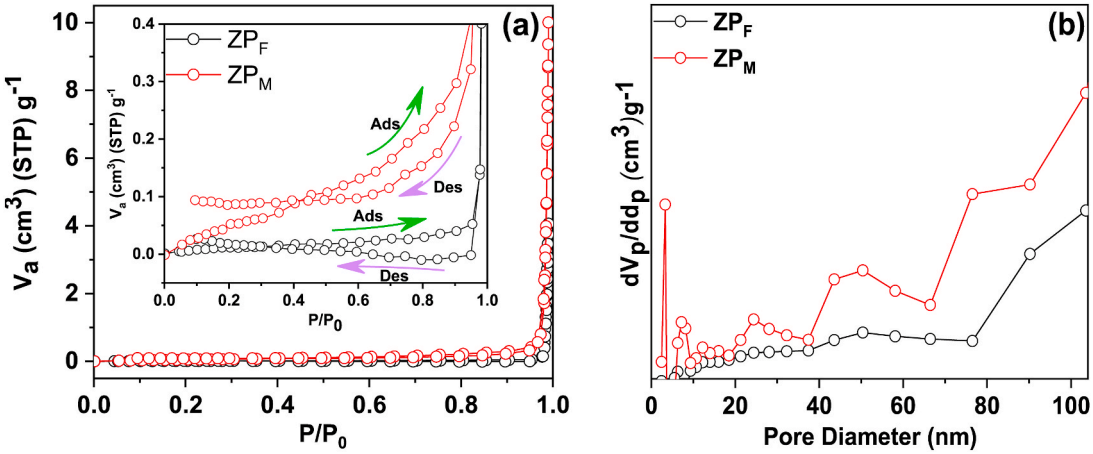

Fig. 9. (a) Nitrogen adsorption-desorption isotherms and (b) BJH pore-size distributions for the prepared flexible ZP_F and ZP_M films. The inset in (a) shows the enlarged view of the nitrogen adsorption/desorption isotherms.

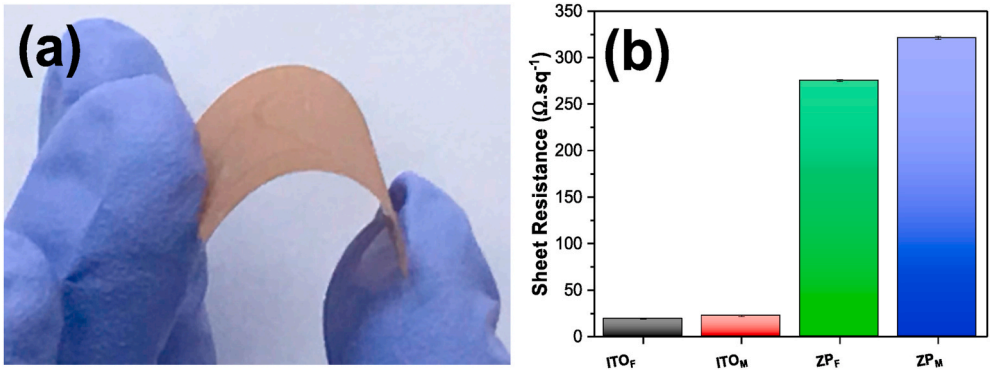

Fig. 10. (a) The optical images of the fabricated flexible ZP_M film. (b) The sheet resistance of the ITO deposited on the flat PET (ITO_F), micropillar PUA (ITO_M), and fabricated flexible films of ZP_F and ZP_M.

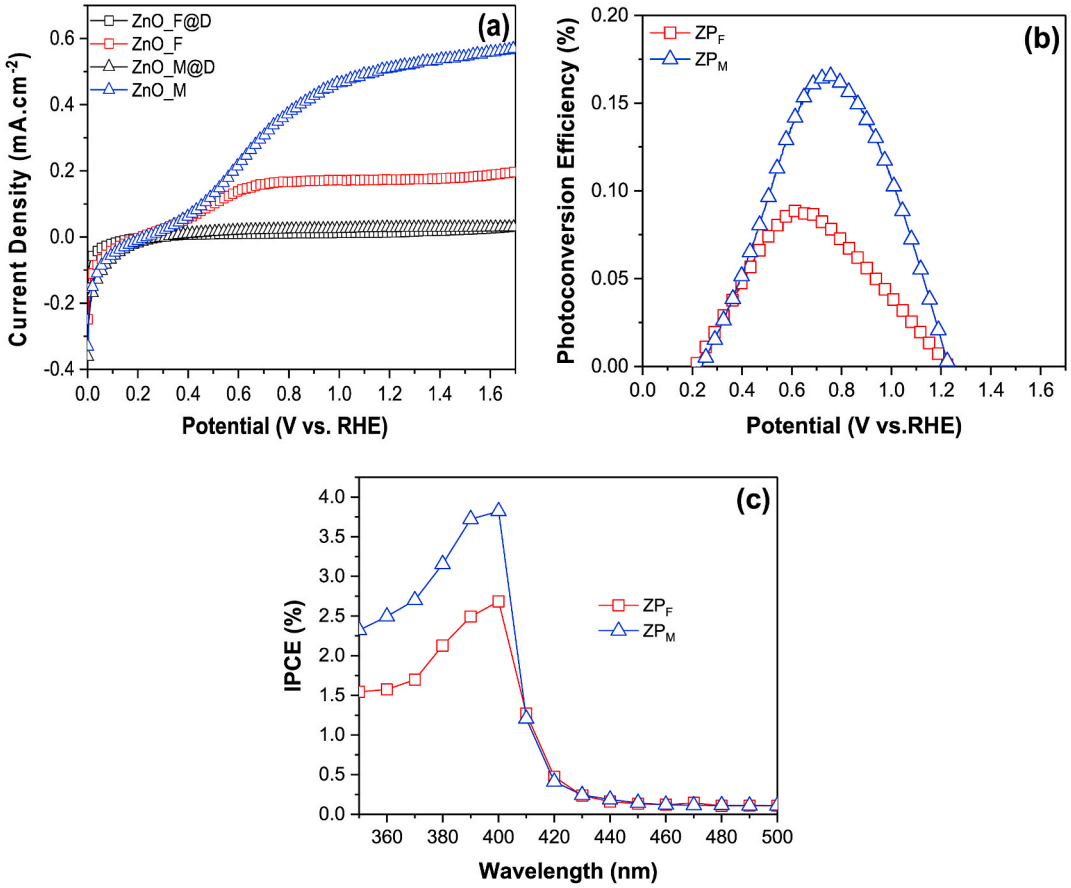

Fig. 11. The PEC performance of the as-fabricated photoanodes of ZP_F and ZP_M: (a) J-V plots recorded in the dark and under illumination at a scan rate of 10 mV s^{-1}, (b) the relationship between the photoconversion efficiency and the applied potential, and (c) IPCE spectra at the wavelength range from 350 to 500 nm.

photoelectrodes based ZP_F and ZP_M were analyzed by the Barrett, Joyner, and Halenda (BJH) isotherm and Brunauer–Emmett–Teller (BET) surface area analysis. Fig. 9a shows the BJH isotherms of the ZP_F and ZP_M films were investigated at 77 K under the nitrogen atmosphere. Both the samples show the type-IV isotherms indicating the mesoporous nature of the fabricated electrodes [48]. The inset in Fig. 9a shows the enlarged region of the BJH isotherms of the ZP_F and ZP_M films. A round "knee", which indicates the approximate location of monolayer formation in which the BET surface area of both samples was calculated. The ZP_F and ZP_M films' calculated surface was found to be ~0.179 and 0.448 m^2 $g^{-1}_{substrate+ZnO}$, respectively. The ZP_F and ZP_M films' surface was normalized to the substrate's total mass and weight and weight of the ZnO NRs on the substrate. Fig. 9b shows the pore size distribution of the ZP_F and ZP_M films. Both the samples show the pores in the range of 2–100 nm; however, the ZP_M film exhibits much more pore size than the ZP_F, which plays a significant role in enhancing the specific surface area.

Fig. 10(a) shows the flexibility of the fabricated ZP_M film. The fabricated photoanode could withstand several hundreds of bending cycles at a bending angle above 90° without any defect. The sheet resistance of the fabricated films was measured by the four-probe method. The sheet resistance of the ITO deposited on the flat PET and micropillar PUA (Fig. 10(b)) was found to be ~18.8 and 22.2 Ω sq^{-1}, respectively. The sheet resistance of the ZP_F and ZP_M were ~275.4 and 321.3 Ω sq^{-1}, respectively.

Table 1
The PEC performance of the proposed ZP_M and ZP_F photoelectrode and that of other published ZnO photoanodes with different structures. The bias corresponding to the photocurrent densities is normalized to RHE.

Structure	Photocurrent density (mA cm^{-2})	Ref.
ZnO NRs	0.18, 1.23 V (vs. RHE)	[49]
ZnO nanotrees	0.38, 1.23 V (vs. RHE)	
ZnO nanorod clusters	0.5, 1.23 V (vs. RHE)	
"Caterpillar-like" branched ZnO nanofibers (BZNs)	0.35, 1.23 V (vs. RHE)	[50]
Vertically-aligned ZnO nanowires (NWs)	0.2, 1.23 V (vs. RHE)	
ZnO nanorod	0.3, 1.23 V (vs. RHE)	[51]
Branched ZnO nanotetrapods	0.19, 1.23 V (vs. RHE)	[52]
Textured porous ZnO plates	0.40, 1.23 V (vs RHE)	[22]
Vertically-aligned ZnO NWs	0.1, 1.23 V (vs. RHE)	[53]
ZnO NRs	0.45, 1.23 V (vs. RHE)	[54]
ZnO NRs	0.14, 1.23 V (vs. RHE)	[55]
ZP_F	0.17, 1.23 V (vs. RHE)	Present
ZP_M	0.52, 1.23 V (vs. RHE)	work

The PEC performance of the fabricated photoanodes based on ZP_F and ZP_M was investigated by measuring the current-voltage (J-V) characteristics using a three-electrode photoelectrochemical water splitting cell under simulated light illumination (100 mW cm^{-2}) in a 0.5 M of Na_2SO_4 aqueous solution (Fig. 11 (a)). Both ZP_F and ZP_M photoanodes showed an almost negligible current density from 0 to 1.7 V vs. RHE in the dark. Thus, the detected current densities were generated by the photoelectrochemical water splitting. Both photoanodes showed similar J-V curves change the trend, that the photocurrent densities were increased with increasing bias potential.

The photocurrent density generated by the ZP_F photoanode was ~0.17 mA cm^{-2}, whereas the ZP_M achieved the photocurrent density of ~0.52 mA cm^{-2} at 1.23 V vs. RHE. The ZP_M photoanode showed ~3 times higher photocurrent density compared to that of the ZP_F photoanode. The obtained photocurrent density of proposed ZP_M and ZP_F compared with the previously reported nanostructured ZnO photoelectrode (Table 1). It indicates that the ZnO NRs grown on the flexible micropatterned substrate are promising for water oxidation. The photoconversion of the photoanode also was estimated as shown in Fig. 11 (b) with Eq. (S5). The optimal photoconversion efficiency of ZP_F and ZP_M photoanode was 0.09, 0.17%, respectively.

To further investigate the fabricated electrodes' photo-conversion efficiency, the incident-photon-to-charge efficiency (IPCE) spectra were recorded in the wavelength range of 300–500 nm with a three-electrode configuration at 0.6 V vs. RHE (Fig. 11c). The photoelectrodes based on ZP_F and ZP_M exhibited a photoresponse in the UV light region and a negligible IPCE in the visible region. The highest IPCE value measured for ZP_M photoelectrode was ~3.8% at a wavelength of 400 nm. The IPCE of the ZP_M photoelectrode was ~1.4 times higher than the ZP_F photoelectrode. The enhanced PEC performance of the ZP_M photoelectrode is attributed to the improvement in charge collection and transport capability, excellent light scattering, and high surface area owing to micropillar structure.

The electrochemical properties of the fabricated photoanodes based on ZP_F and ZP_M were investigated by electrochemical impedance measurement in the frequency range of 10^5–10^{-1} Hz using an amplitude of 10 mV at the open circuit potential in the dark condition (Fig. 12 (a)). The Nyquist plots for all the photoanodes showed a semicircle and a straight sloping line at high and low frequencies, respectively. Further, the EIS experimental data were fitted with the standard electrical equivalent circuit (Table 2). The equivalent circuit includes a parallel RC unit (high frequency "surface resistance") for the double layer in parallel with a finite-length Warburg unit (low frequency "diffusion") for a finite length capacitor cutoff. The factor R_s is representing the total resistance arises from the bulk semiconductor, contacts, electrode wires, and electrolyte [56]. The CPE and R_{ct} are representing the double-layer capacitance and charge transfer resistance of the device, respectively. The Warburg (W) describes the semi-infinite diffusion process of the reactive species on the surface of the electrode [57]. The calculated charge transfer resistance (R_{ct}) in double-layer capacitance of the ZP_F and ZP_M based photoanodes were found to be ~4.6×10^6 and 3.1×10^3, respectively. The ZP_M photoanode exhibited ~3 orders of lower double-layer capacitance than the ZP_F. The lower double-layer capacitance is another reason for the enhanced PEC performance of the ZP_M photoanode.

The electrochemical active surface area (ECSA) of the fabricated ZP_F and ZP_M photoanodes was calculated using the cyclic voltammetry analysis to analyze the overall active sites of the photoanodes at the solid-liquid interface. The ECSA was evaluated from the electrochemical

Table 2
The electrochemical properties of the fabricated photoanodes based on ZP_F and ZP_M calculated by fitting the equivalent circuit model obtained from the EIS

Nyquist plots. 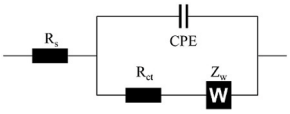

Photoanode	R_s (Ω cm^{-2})	R_{ct} (Ω cm^{-2})	Q-Y_o (Ω^{-1} cm^{-2} S^n)	Q-n	Y_0 (Ω^{-1} cm^{-2} $S^{0.5}$)
ZP_F	31.7	4.6×10^6	1.6×10^{-5}	0.79	2.0×10^{-5}
ZP_M	30.8	3.1×10^3	1.2×10^{-4}	0.80	5.5×10^{-5}

Y_0 is the admittance value, which is inversely proportional to the Warburg coefficient.

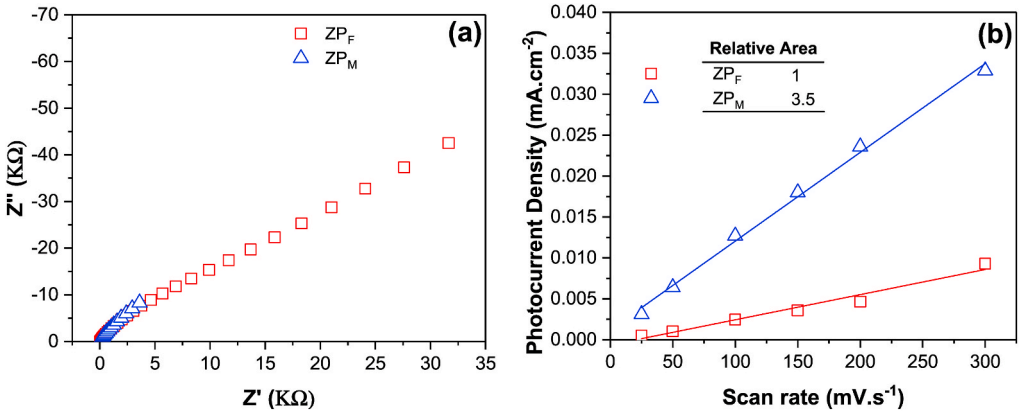

Fig. 12. (a) EIS measured under illumination condition at open circuit voltage over a frequency range from 10^5 to 10^{-1} Hz with an AC voltage at 10 mV and (b) the electrochemical active surface area for the ZP_F and ZP_M photoanodes.

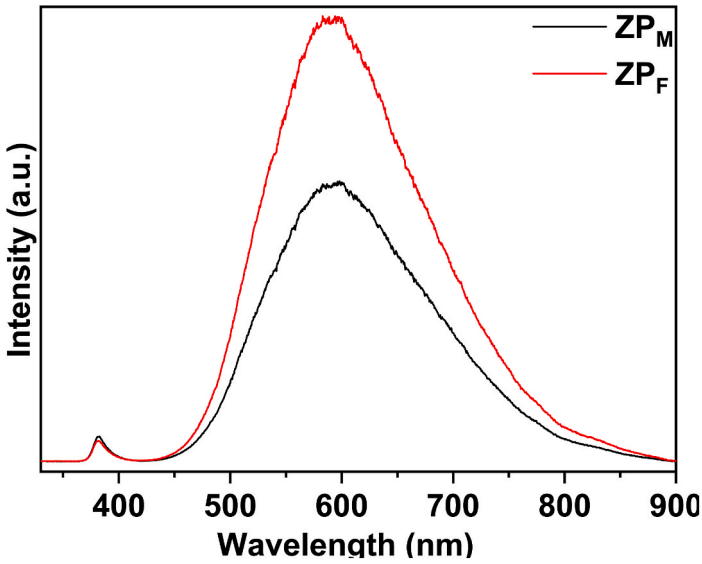

Fig. 13. PL spectroscopy analysis of as-prepared flexible ZP_F and ZP_M films.

double-layer capacitance (C_{dl}) by measuring CVs in the non-Faradaic region (0.45–0.55 V vs. RHE). Fig. 12(b) shows the linear relationship between the capacitive current as a function of the scan rate at 0.5 V vs. RHE. The C_{dl} of the ZP_F and ZP_M photoanodes were obtained from the slope of the linear portion of the plots. The calculated C_{dl} of the ZP_M photoanode was showed ~3.5 times of electrochemically active surface area compared to that of the ZP_F photoanode. The higher ESCA of the ZP_M photoanode further confirms that the formation of the micropattern technique is an effective way to increase the electrochemically active surface area, which is an imperative factor for the photoanodes in PEC water splitting.

The photoluminescence (PL) spectroscopy analysis was carried out to investigate the electronic, optical, and photochemical properties of the ZP_F and ZP_M photoanodes (Fig. 13). The fabricated photoelectrodes show the emission peaks at ~381 nm and 590 nm. The peak located at 381 nm is attributed to the free excitons' recombination through an exciton-exciton collision process [58]. The other peak at 590 nm corresponds to the oxygen vacancies or interstitial zinc ions of ZnO [59,60]. The PL intensity of ZP_M was quenched compared to the ZP_F photoanode indicating the faster electron transfer and higher charge carrier separation of photogenerated e-h pairs, thus improving the PEC efficiency of the ZP_M electrode.

The PEC characteristics established that the formation of ordered micropatterned topography has been successful in improving the efficiency of the ZP_M photoanode. The enhanced PEC performance of the ZP_M photoanode is attributed to the (i) high surface area, (ii) excellent light trapping effect, (iii) faster electron transfer and higher charge carrier separation of photogenerated e-h pairs, (iv) lower charge transfer resistance and (v) high electrochemically active surface area. The actual surface area of the micropatterned substrate is increased by ~15.5% than the flat substrate through the geometrical calculation. Besides, the periodically arranged micropillars coated with ZnO significantly increase the light trapping effect, which further increases the PEC performance of the ZP_M photoanode. As observed from the UVDRS analysis, the vertically aligned ordered micropatterned surface exhibits a better light absorption than the flat surface photoelectrode. Hence, the ZP_M photoanode absorbed more light and significantly produced a higher number of photogenerated charge carriers. The PL spectrum of the ZP_M photoanode is quenched compared to the ZP_F photoanode indicating the faster electron transfer and higher charge carrier separation of photogenerated e-h pairs; thus, the ZP_M showed much lower charge transfer resistance. The ECSA of the ZP_M photoanode is higher than the ZP_F photoanode signifying the higher interface between the electrode surface and the electrolyte accompanying superior light absorption. The synergetic effect between the vertically aligned ordered micropatterned surface and the one dimensional ZnO nanorods accelerate the efficiency during PEC analysis.

4. Conclusions

The ZnO NRs based photoanodes were prepared on a flexible micropatterned and flat PUA substrate. The micropatterned PUA flexible substrate was fabricated by the modified photolithography technique. A thin layer of ITO was deposited on the PUA surface by the RF-magnetron spurting technique to collect the electrical signal. The ZnO NRs arrays based photoanodes were prepared by the facile seed layer and hydrothermal method. The photocurrent density generated by the ZP_F and ZP_M photoanodes were ~0.17 and 0.52 mA cm^{-2}, respectively, at 1.23 V vs. RHE. The enhanced performance was attributed to the improved light absorption, lower double-layer capacitance, and higher ECSA of the ZP_M photoanodes. Although the attained photocurrents are small compared to that of the other reported ZnO based photoanodes, this work opens up a new way of designing flexible photoanodes on the patterned substrate.

Credit authorship contribution statement

Tian-Feng Hou: Conceptualization, Methodology, Software, Formal analysis, writing manuscript, Resources, Writing - original draft. Arunkumar Shanmugasundaram: Formal analysis, Writing-review & editing. Indrajit V. Bagal: formal analysis, Sang-Wan Ryub & Dong-Weon Lee: Conceptualization, Supervision, Funding acquisition, Review.

Declaration of competing interest

The authors declare that they have no known competing financial interests or personal relationships that could have appeared to influence the work reported in this paper.

Acknowledgments

This work was financially supported by the National Research Foundation of Korea (NRF) grant funded by the Korean government (MSIT) (No.2017R1E1A1A01074550) and Basic Science Research Program through the National Research Foundation of Korea(NRF) funded by the Ministry of Education (No. 2020R1I1A1A01073562).

Appendix A. Supplementary data

Supplementary data to this article can be found online at https://doi.org/10.1016/j.mssp.2020.105445.

References

[1] Y. Naimi, A. Antar, Hydrogen generation by water electrolysis, in: Advances in Hydrogen Generation Technologies, 2018, p. 1, https://doi.org/10.5772/intechopen.76814.

[2] T. Bak, J. Nowotny, M. Rekas, C.C. Sorrell, Photo-electrochemical hydrogen generation from water using solar energy. Materials-related aspects, Int. J. Hydrogen Energy 27 (10) (2002) 991–1022, https://doi.org/10.1016/S0360-3199(02)00022-8.

[3] A. Fujishima, Electrochemical photolysis of water at a semiconductor electrode, Nature 238 (5358) (1972) 37–38, https://doi.org/10.1038/238037a0.

[4] M.G. Walter, E.L. Warren, J.R. McKone, S.W. Boettcher, Q. Mi, E.A. Santori, N. S. Lewis, Solar water splitting cells, Chem. Rev. 110 (11) (2010) 6446–6473, https://doi.org/10.1021/cr1002326.

[5] I.S. Cho, Z. Chen, A.J. Forman, D.R. Kim, P.M. Rao, T.F. Jaramillo, X. Zheng, Branched TiO_2 nanorods for photoelectrochemical hydrogen production, Nano Lett. 11 (11) (2011) 4978–4984, https://doi.org/10.1021/nl2029392.

[6] Y. Yang, D. Xu, Q. Wu, P. Diao, Cu_2O/CuO bilayered composite as a high-efficiency photocathode for photoelectrochemical hydrogen evolution reaction, Sci. Rep. 6 (2016) 35158, https://doi.org/10.1038/srep35158 (2016).

[7] Y.-K. Hsu, Y.-C. Chen, Y.-G. Lin, Novel ZnO/Fe_2O_3 core–shell nanowires for photoelectrochemical water splitting, ACS Appl. Mater. Interfaces 7 (25) (2015) 14157–14162, https://doi.org/10.1021/acsami.5b03921.

[8] L. Yan, W. Zhao, Z. Liu, 1D ZnO/$BiVO_4$ heterojunction photoanodes for efficient photoelectrochemical water splitting, Dalton Trans. 45 (28) (2016) 11346–11352, https://doi.org/10.1039/C6DT02027E.

[9] J. Su, L. Guo, N. Bao, C.A. Grimes, Nanostructured WO_3/$BiVO_4$ heterojunction films for efficient photoelectrochemical water splitting, Nano Lett. 11 (5) (2011) 1928–1933, https://doi.org/10.1021/nl2000743.

[10] M.G. Lee, J.S. Park, H.W. Jang, M.G. Lee, J.S. Park, H.W. Jang, Solution-processed metal oxide thin film nanostructures for water splitting photoelectrodes: a review, J. Korean Ceram. Soc. 55 (3) (2018) 185–202, https://doi.org/10.4191/kcers.2018.55.3.08.

[11] Shaoce Zhang, Zhifeng Liu, Mengnan Ruan, Zhengang Guo, E. Lei, Wei Zhao, Dan Zhao, Xiangfeng Wu, Daimei Chen, Enhanced piezoelectric-effect-assisted photoelectrochemical performance in ZnO modified with dual cocatalysts, Appl. Catal., B 262 (2020) 118279, https://doi.org/10.1016/j.apcatb.2019.118279.

[12] S. Wei, Y. Chen, Y. Ma, Z. Shao, Fabrication of CuO/ZnO composite films with cathodic co-electrodeposition and their photocatalytic performance, J. Mol. Catal. Chem. 331 (1) (2010) 112–116, https://doi.org/10.1016/j.molcata.2010.08.011.

[13] A. Ghobadi, T.G.U. Ghobadi, F. Karadas, E. Ozbay, Angstrom thick ZnO passivation layer to improve the photoelectrochemical water splitting performance of a TiO_2 nanowire photoanode: the role of deposition temperature, Sci. Rep. 8 (1) (2018) 16322, https://doi.org/10.1038/s41598-018-34248-3.

[14] A. Janotti, C.G. Van de Walle, Fundamentals of zinc oxide as a semiconductor, Rep. Prog. Phys. 72 (12) (2009) 126501, https://doi.org/10.1088/0034-4885/72/12/126501.

[15] A. Soudi, P. Dhakal, Y. Gu, Diameter dependence of the minority carrier diffusion length in individual ZnO nanowires, Appl. Phys. Lett. 96 (25) (2010) 253115, https://doi.org/10.1063/1.3456390.

[16] Y. Mao, Y. Cheng, J. Wang, H. Yang, M. Li, J. Chen, M. Chao, Y. Tong, E. Liang, Amorphous NiO electrocatalyst overcoated ZnO nanorod photoanodes for enhanced photoelectrochemical performance, New J. Chem. 40 (1) (2016) 107–112, https://doi.org/10.1039/C5NJ01815C.

[17] C. Ma, Z. Liu, Q. Cai, C. Han, Z. Tong, ZnO photoelectrode simultaneously modified with Cu_2O and Co-Pi based on broader light absorption and efficiently photogenerated carrier separation, Inorg. Chem. Front. 5 (10) (2018) 2571–2578, https://doi.org/10.1039/C8QI00596F.

[18] M. Wang, F. Ren, J. Zhou, G. Cai, L. Cai, Y. Hu, D. Wang, Y. Liu, L. Guo, S. Shen, N doping to ZnO nanorods for photoelectrochemical water splitting under visible light: engineered impurity distribution and terraced band structure, Sci. Rep. 5 (2015) 12925, https://doi.org/10.1039/C9DT02564B.

[19] H. Kim, K. Yong, Highly efficient photoelectrochemical hydrogen generation using a quantum dot coupled hierarchical ZnO nanowires array, ACS Appl. Mater. Interfaces 5 (24) (2013) 13258–13264, https://doi.org/10.1021/am404259y.

[20] M. Ding, N. Yao, C. Wang, J. Huang, M. Shao, S. Zhang, P. Li, X. Deng, X. Xu, ZnO@CdS core-shell heterostructures: fabrication, enhanced photocatalytic, and photoelectrochemical performance, Nanoscale Res. Lett. 11 (1) (2016) 205, https://doi.org/10.1186/s11671-016-1432-7.

[21] Y. Liu, Y. Gu, X. Yan, Z. Kang, S. Lu, Y. Sun, Y. Zhang, Design of sandwich-structured ZnO/ZnS/Au photoanode for enhanced efficiency of photoelectrochemical water splitting, Nano Res. 8 (9) (2015) 2891–2900, https://doi.org/10.1007/s12274-015-0794-y.

[22] S. Emin, M. Fanetti, F.F. Abdi, D. Lisjak, M. Valant, R. van de Krol, B. Dam, Photoelectrochemical properties of cadmium chalcogenide-sensitized textured porous zinc oxide plate electrodes, ACS Appl. Mater. Interfaces 5 (3) (2013) 1113–1121, https://doi.org/10.1021/am3027986.

[23] X. Zhang, Y. Liu, Z. Kang, 3D branched ZnO nanowire arrays decorated with plasmonic Au nanoparticles for high-performance photoelectrochemical water splitting, ACS Appl. Mater. Interfaces 6 (6) (2014) 4480–4489, https://doi.org/10.1021/am500234v.

[24] W. Yang, Y. Yu, M.B. Starr, X. Yin, Z. Li, A. Kvit, S. Wang, P. Zhao, X. Wang, Ferroelectric polarization-enhanced photoelectrochemical water splitting in TiO_2–$BaTiO_3$ core–shell nanowire photoanodes, Nano Lett. 15 (11) (2015) 7574–7580, https://doi.org/10.1021/acs.nanolett.5b03988.

[25] Y. Chen, L. Wang, R. Gao, Y.C. Zhang, J.J. Zou, Polarization-enhanced direct Z-scheme ZnO-WO_{3-x} nanorod arrays for efficient piezoelectric-photoelectrochemical water splitting, Appl. Catal., B 259 (2019) 118079, https://doi.org/10.1016/j.apcatb.2019.118079.

[26] S. Li, Z. Shi, Z. Tang, X. Li, Comparison of ITO, In_2O_3: Zn and In_2O_3: H transparent conductive oxides as front electrodes for silicon heterojunction solar cell applications, Vacuum 145 (2017) 262–267, https://doi.org/10.1016/j.vacuum.2017.09.011.

[27] M.A. Martinez, J. Herrero, M.T. Gutierrez, Deposition of transparent and conductive Al-doped ZnO thin films for photovoltaic solar cells, Sol. Energy Mater. Sol. Cells 45 (1) (1997) 75–86, https://doi.org/10.1016/S0927-0248(96)00066-9.

[28] Y. Wei, Z. Wang, J. Su, L. Guo, Metal-free flexible protonated g-C_3N_4/carbon dots photoanode for photoelectrochemical water splitting, ChemElectroChem 5 (19) (2018) 2734–2737, https://doi.org/10.1002/celc.201800550.

[29] S. Singh, N. Khare, Flexible PVDF/Cu/PVDF-$NaNbO_3$ photoanode with ferroelectric properties: an efficient tuning of photoelectrochemical water splitting with electric field polarization and piezophototronic effect, Nano Energy 42 (2017) 173–180, https://doi.org/10.1016/j.nanoen.2017.10.061.

[30] L.T. Quynh, C.N. Van, W.Y. Tzeng, C.-W. Huang, Y.-H. Lai, J.-W. Chen, K.-A. Tsai, C.L. Wu, W.-W. Wu, C.W. Luo, Flexible heteroepitaxy photoelectrode for photo-electrochemical water splitting, ACS Appl. Energy Mater. 1 (8) (2018) 3900–3907, https://doi.org/10.1021/acsaem.8b00645.

[31] H. Li, S. Xiao, J. Zhou, J. Zhao, F. Liu, G. Li, D. Zhang, A flexible CdS nanorods-carbon nanotubes/stainless steel mesh photoanode for boosted photoelectrocatalytic hydrogen evolution, Chem. Commun. (Camb.) 55 (19) (2019) 2741–2744, https://doi.org/10.1039/C9CC00050J.

[32] T.-F. Hou, A. Shanmugasundaram, M.A. Hassan, M.A. Johar, S.-W. Ryu, D.-W. Lee, ZnO/Cu_2O-decorated rGO: heterojunction photoelectrode with improved solar water splitting performance, Int. J. Hydrogen Energy 44 (35) (2019) 19177–19192, https://doi.org/10.1016/j.ijhydene.2018.05.105.

[33] M.G. Faraj, K. Ibrahim, Optical and structural properties of thermally evaporated zinc oxide thin films on polyethylene terephthalate substrates, Int. J. Polym. Sci. 2011 (2011) 302843, https://doi.org/10.1155/2011/302843.

[34] M. Thirumoorthi, J. Thomas Joseph Prakash, Structure, optical and electrical properties of indium tin oxide ultra thin films prepared by jet nebulizer spray pyrolysis technique, J. Asian Ceram. Soc. 4 (1) (2016) 124–132, https://doi.org/10.1016/j.jascer.2016.01.001.

[35] S. Arunkumar, T. Hou, Y.-B. Kim, B. Choi, S.H. Park, S. Jung, D.-W. Lee, Au decorated ZnO hierarchical architectures: facile synthesis, tunable morphology and enhanced CO detection at room temperature, Sens. Actuators, B 243 (2017) 990–1001, https://doi.org/10.1016/j.snb.2016.11.152.

[36] S. Arunkumar, B. Ramireddy, J. Yun-Jin, P. Jongsung, K. Young-Bae, C. Byungchul, P.S. Han, J. Seunghun, L. Dong-Weon, Facile in-situ formation of rGO/ZnO nanocomposite: photocatalytic remediation of organic pollutants under solar illumination, Mater. Chem. Phys. 218 (2018) 218–228, https://doi.org/10.1016/j.matchemphys.2018.07.046.

[37] J. Gao, Q. Zhao, Y. Sun, G. Li, J. Zhang, D. Yu, A novel way for synthesizing phosphorus-doped Zno nanowires, Nanoscale Res. Lett. 6 (1) (2011) 45, https://doi.org/10.1007/s11671-010-9805-9.

[38] N. Tiwari, S. Kumar, A.K. Ghosh, S. Chatterjee, S.N. Jha, D. Bhattacharyya, Structural investigations of (Mn, Dy) co-doped ZnO nanocrystals using X-ray absorption studies, RSC Adv. 7 (89) (2017) 56662–56675, https://doi.org/10.1039/C7RA10748J.

[39] Q.-Q. Chang, Y.-W. Cui, H.-H. Zhang, F. Chang, B.-H. Zhu, S.-Y. Yu, C-doped ZnO decorated with Au nanoparticles constructed from the metal–organic framework ZIF-8 for photodegradation of organic dyes, RSC Adv. 9 (22) (2019) 12689–12695, https://doi.org/10.1039/C8RA09985E.

[40] A. Shanmugasundaram, V. Gundimeda, T. Hou, D.W. Lee, Realizing synergy between In2O3 nanocubes and nitrogen-doped reduced graphene Oxide: an excellent nanocomposite for the selective and sensitive detection of CO at ambient temperatures, ACS Appl. Mater. Interfaces 9 (37) (2017) 31728–31740, https://doi.org/10.1021/acsami.7b06253.

[41] A. Kushwaha, M. Aslam, Hydrogen-incorporated ZnO nanowire films: stable and high electrical conductivity, J. Phys. D Appl. Phys. 46 (48) (2013) 485104, https://doi.org/10.1088/0022-3727/46/48/485104.

[42] Y. Chen, X.L. Xu, G.H. Zhang, H. Xue, S.Y. Ma, Blue shift of optical band gap in Er-doped ZnO thin films deposited by direct current reactive magnetron sputtering technique, Phys. E (Amsterdam, Neth.) 42 (5) (2010) 1713–1716, https://doi.org/10.1016/j.physe.2010.01.029.

[43] M. Yadav, V. Singh, Y.C. Sharma, Methyl transesterification of waste cooking oil using a laboratory synthesized reusable heterogeneous base catalyst: process optimization and homogeneity study of catalyst, Energy Convers. Manage. 148 (2017) 1438–1452, https://doi.org/10.1016/j.enconman.2017.06.024.

[44] A. Shanmugasundaram, N.D. Chinh, Y.-J. Jeong, T.F. Hou, D.-S. Kim, D. Kim, Y.-B. Kim, D.-W. Lee, Hierarchical nanohybrids of B-and N-codoped graphene/mesoporous NiO nanodisks: an exciting new material for selective sensing of H_2S at near ambient temperature, J. Mater. Chem. A 7 (15) (2019) 9263–9278, https://doi.org/10.1039/C9TA00755E.

[45] M. Schumm, ZnO-based semiconductors studied by Raman spectroscopy: semimagnetic alloying, doping, and nanostructures. https://www.svh-verlag.de, 2008, 188.
[46] M. Silambarasan, S. Saravanan, T. Soga, Effect of Fe-doping on the structural, morphological and optical properties of ZnO nanoparticles synthesized by solution combustion process, Phys. E (Amsterdam, Neth.) 71 (2015) 109–116, https://doi.org/10.1016/j.physe.2015.04.002.
[47] Y. Song, S. Zhang, C. Zhang, Y. Yang, K. Lv, Raman spectra and microstructure of Zinc oxide irradiated with swift heavy ion, Crystals 9 (8) (2019) 395, https://doi.org/10.3390/cryst9080395.
[48] K.S.W. Sing, Reporting physisorption data for gas/solid systems with special reference to the determination of surface area and porosity, Pure Appl. Chem. 54 (11) (1982) 2201–2218, https://doi.org/10.1351/pac198254112201.
[49] X. Ren, A. Sangle, S. Zhang, S. Yuan, Y. Zhao, L. Shi, R.L.Z. Hoye, S. Cho, D. Li, J. L. MacManus-Driscoll, Photoelectrochemical water splitting strongly enhanced in fast-grown ZnO nanotree and nanocluster structures, J. Mater. Chem. A 4 (26) (2016) 10203–10211, https://doi.org/10.1039/C6TA02788A.
[50] Q. Li, X. Sun, K. Lozano, Y. Mao, Facile and scalable synthesis of “caterpillar-like” ZnO nanostructures with enhanced photoelectrochemical water-splitting effect, J. Phys. Chem. C 118 (25) (2014) 13467–13475, https://doi.org/10.1021/jp503155c.
[51] M. Wu, W.-J. Chen, Y.-H. Shen, F.-Z. Huang, C.-H. Li, S.-K. Li, In situ growth of matchlike ZnO/Au plasmonic heterostructure for enhanced photoelectrochemical water splitting, ACS Appl. Mater. Interfaces 6 (17) (2014) 15052–15060, https://doi.org/10.1021/am503044f.
[52] Y. Qiu, K. Yan, H. Deng, S. Yang, Secondary branching and nitrogen doping of ZnO nanotetrapods: building a highly active network for photoelectrochemical water splitting, Nano Lett. 12 (1) (2011) 407–413, https://doi.org/10.1021/nl2037326.
[53] C.S. Yaw, Q. Ruan, J. Tang, A.K. Soh, M.N. Chong, A Type II nn staggered orthorhombic V_2O_5/monoclinic clinobisvanite $BiVO_4$ heterojunction photoanode for photoelectrochemical water oxidation: fabrication, characterisation and experimental validation, Chem. Eng. J. 364 (2019) 177–185, https://doi.org/10.1016/j.cej.2019.01.179.
[54] T. Wang, R. Lv, P. Zhang, C. Li, J. Gong, Au nanoparticle sensitized ZnO nanopencil arrays for photoelectrochemical water splitting, Nanoscale 7 (1) (2015) 77–81, https://doi.org/10.1039/C4NR03735A.
[55] Y. Liu, X. Yan, Z. Kang, Y. Li, Y. Shen, Y. Sun, L. Wang, Y. Zhang, Synergistic effect of surface plasmonic particles and surface passivation layer on ZnO nanorods array for improved photoelectrochemical water splitting, Sci. Rep. 6 (2016) 29907, https://doi.org/10.1038/srep29907 (2016).
[56] Z. Chen, H.N. Dinh, E. Miller, Photoelectrochemical Water Splitting: Standards, Experimental Methods, and Protocols, Springer, New York, 2013.
[57] W. Zhao, Z. Ai, J. Dai, M. Zhang, Enhanced photocatalytic activity for H_2 evolution under irradiation of UV–Vis light by Au-modified nitrogen-doped TiO_2, PLoS One 9 (8) (2014), e103671, https://doi.org/10.1371/journal.pone.0103671.
[58] D. Chu, Y. Masuda, T. Ohji, K. Kato, Formation and photocatalytic application of ZnO nanotubes using aqueous solution, Langmuir ACS J. Surfaces Colloids 26 (4) (2010) 2811–2815, https://doi.org/10.1021/la902866a.
[59] Q. Jiang, Z.Y. Wu, Y.M. Wang, Y. Cao, C.F. Zhou, J.H. Zhu, Fabrication of photoluminescent ZnO/SBA-15 through directly dispersing zinc nitrate into the as-prepared mesoporous silica occluded with template, J. Mater. Chem. 16 (16) (2006) 1536–1542, https://doi.org/10.1039/b516061h.
[60] Pita Kantisara, Baudin Pierre, Vinh Quang, Roy Vu, Christophe Aad, Annealing temperature and environment effects on ZnO nanocrystals embedded in SiO_2: a photoluminescence and TEM study, Nanoscale Res. Lett. 8 (2013) 517, https://doi.org/10.1186/1556-276X-8-517.